Inorganic Chemistry
Article

Inorg. Chem. **2010**, *49*, 11309–11316 **11309**
DOI: 10.1021/ic1007796

How Does the Synthesis Temperature Impact Hybrid Organic−Inorganic Molybdate Material Design?

Rémi Dessapt,* Daniel Kervern, Martine Bujoli-Doeuff, Philippe Deniard, Michel Evain, and Stéphane Jobic

Institut des Matériaux Jean Rouxel, Université de Nantes, CNRS, 2 rue de la Houssinière,
BP 32229, 44322 Nantes, France

Received April 22, 2010

We investigate the reactivity of MoO_4^{2-} toward six organoammonium cations $^{+}(Me_{3-x}H_xN)(CH_2)_2(NH_yMe_{3-y})^{+}$ (x, $y = 1-3$) at different synthesis temperatures ranging from 70 to 180 °C. A total of 16 hybrid organic−inorganic materials have been synthesized at an initial pH of 2, via ambient pressure and hydrothermal routes, namely, $(H_2en)[Mo_3O_{10}]\cdot H_2O$ (**1**), $(H_2en)[Mo_3O_{10}]$ (**2**), $(H_2en)[Mo_5O_{16}]$ (**3**), $(H_2MED)_2[Mo_8O_{26}]\cdot 2H_2O$ (**4**), $(H_2MED)[Mo_5O_{16}]$ (**5**), $(N,N\text{-}H_2DMED)_2[Mo_8O_{26}]\cdot 2H_2O$ (**6**), $(N,N\text{-}H_2DMED)_2[Mo_8O_{26}]\cdot 2H_2O$ (**7**), $(N,N'\text{-}H_2DMED)_2[Mo_8O_{26}]$ (**8**), $(N,N'\text{-}H_2DMED)[Mo_5O_{16}]$ (**9**), $(H_2TriMED)_2[Mo_8O_{26}]\cdot 4H_2O$ (**10**), $(H_2TriMED)_2[Mo_8O_{26}]\cdot 2H_2O$ (**11**), $(H_2TriMED)[Mo_7O_{22}]$ (**12**), $(H_2TMED)_2[Mo_8O_{26}]\cdot 2H_2O$ (**13**), $(H_2TMED)_2[Mo_8O_{26}]$ (**14**), $(H_2TMED)_2[Mo_8O_{26}]$ (**15**), and $(H_2TMED)[Mo_7O_{22}]$ (**16**). All of these compounds contain different polyoxomolybdate (Mo-POM) blocks, i.e., discrete $\beta\text{-}[Mo_8O_{26}]^{4-}$ blocks in **6**, **10**, **13**, **14**, ${}^{1}/_{\infty}[Mo_3O_{10}]^{2-}$, and ${}^{1}/_{\infty}[Mo_8O_{26}]^{4-}$ polymeric chains in **1**, **2**, **4**, **7**, **8**, and **15**, respectively, and ${}^{2}/_{\infty}[Mo_5O_{16}]^{2-}$ and ${}^{2}/_{\infty}[Mo_7O_{22}]^{2-}$ layers in **3**, **5**, **9**, **12**, and **16**, respectively. The structures of **5**, **9**, and **14** have been resolved by single-crystal X-ray analyses. The characterization of the different Mo-POM blocks in **1**−**16** by Fourier transform Raman spectroscopy is reported. The impact of the synthesis temperature on both the composition and topology of the Mo-POM blocks is highlighted.

1. Introduction

The use of polyoxometalates[1] and polyoxothiometalates[2] as anionic building blocks to generate crystallized hybrid organic−inorganic materials has been largely demonstrated in the recent past. These materials have attracted considerable interest because of their wide diversity of structures and properties. The assembly of isopolyoxomolybdates (Mo-POMs) and organoammonium cations (OACs) via weak interactions (e.g., van der Waals, electrostatic, or hydrogen bonds) is a subclass of this rich family. The topological diversity of both OACs and Mo-POM blocks can be used in numerous self-assembling processes, which may trigger the design of a large range of original hybrid frameworks with tunable dimensionality.

Materials based on Mo-POMs are of great interest for optical applications.[3] Formally, their optical properties are drastically correlated to their composition and architecture. For example, in photochromic materials based on Mo-POMs and OACs, the optical band gaps in the ground state such as the UV-photogenerated coloration only depend on the topology of the Mo-POM block, while the nature of the OACs strongly dictates the kinetics of the color change.[4,5] Hence, anticipating the design of new hybrid organic−inorganic materials should allow one to predict and monitor their optical properties. Such a task needs (i) to anticipate the stabilization of a specific Mo-POM block from a molybdenum source and a given OAC and (ii) to control the organic−inorganic interface, i.e., the hydrogen-bonding subnetwork. Unfortunately, this remains a hard challenge to achieve. Indeed, it implies to identify the chemical forces driving the molybdenum framework condensation, such as the self-assembling processes. Nowadays, at least four adjustable parameters, i.e., the pH, the nature of the OAC, the

---

*To whom correspondence should be addressed. E-mail: remi.dessapt@cnrs-imn.fr. Tel: +33 2 40 37 39 53. Fax: +33 2 40 37 39 95.

(1) (a) Reinoso, S.; Bassil, B. S.; Barsukova, M.; Kortz, U. *Eur. J. Inorg. Chem.* **2010**, 2537–2542. (b) Bao, Y.-Y.; Bi, L.-H.; Wu, L.-X.; Mal, S. S.; Kortz, U. *Langmuir* **2009**, *25*, 13000–13006. (c) Akutagawa, T.; Endo, D.; Noro, S.-I.; Cronin, L.; Nakamura, T. *Coord. Chem. Rev.* **2007**, *251*, 2547–2561. (d) Miras, H. N.; Long, D.-L.; Kögerler, P.; Cronin, L. *Dalton Trans.* **2008**, 214–221. (e) Long, D.-L.; Streb, C.; Song, Y.-F.; Mitchell, S.; Cronin, L. *J. Am. Chem. Soc.* **2008**, *130*, 1830–1832. (f) Long, D.-L.; Burkholder, E.; Cronin, L. *Chem. Soc. Rev.* **2007**, *36*, 105–121. (g) Mialane, P.; Zhang, G.; Mbomekalle, I. M.; Yu, P.; Compain, J.-D.; Dolbecq, A.; Marrot, J.; Sécheresse, F.; Keita, B.; Nadjo, L. *Chem.—Eur. J.* **2010**, *16*, 5572–5576.

(2) (a) Sokolov, M. N.; Kalinina, I. V.; Peresypkina, E. V.; Cadot, E.; Tkachev, S. V.; Fedin, V. P. *Angew. Chem., Int. Ed.* **2008**, *47*, 1465–1468. (b) Duval, S.; Floquet, S.; Simonnet-Jegat, C.; Marrot, J.; Biboum, R. N.; Keita, B.; Nadjo, L.; Haouas, M.; Taulelle, F.; Cadot, E. *J. Am. Chem. Soc.* **2010**, *132*, 2069–2077.

(3) Yamase, T. *Chem. Rev.* **1998**, *98*, 307–325.

(4) Coué, V.; Dessapt, R.; Bujoli-Doeuff, M.; Evain, M.; Jobic, S. *Inorg. Chem.* **2007**, *46*, 2824–2835.

(5) Dessapt, R.; Collet, M.; Coué, V.; Bujoli-Doeuff, M.; Jobic, S.; Lee, C.; Whangbo, M.-H. *Inorg. Chem.* **2009**, *48*, 574–580.

molybdenum concentration, and the organic/molybdenum ratio, have been unambiguously identified to drastically impact the composition and architecture of the final supramolecular assemblies. However, the effects of these different parameters have been unequally investigated up to now, and an understanding of the synthesis conditions−structure relationships is still far from complete.

A powerful method to obtain hybrid materials containing Mo-POM blocks consists of controlled acidification of an aqueous solution containing MoO_4^{2-} anions and OACs. The pH dependence of the Mo-POM compositions is well-known and documented.[6,7] The speciation diagrams of molybdate solutions can then be useful to correlating the molybdate composition in the solid state with the pH value of the solution.[4,8] However, the composition and topology of the Mo-POM blocks in the solid state can mismatch those predicted from the solution. This is essentially because of OACs not only acting as passive charge-compensating counterions but also directing the condensation of the Mo^{6+}-centered polyhedra in solution, through the establishment of complex and unpredictable hydrogen-bonding interactions with the soluble intermediaries. Hence, the pH alone is not sufficient to anticipate the design of hybrid materials.

Recently, systematic composition space-analysis diagrams from molybdate solutions containing different OACs have pertinently shown that, at constant pH and temperature values, the molybdenum concentration and organic/molybdenum ratio strongly impact the composition of the Mo-POM blocks in the hybrid materials.[9−11] For example, octamolybdate and pentamolybdate blocks are often stabilized in molybdenum-rich reactions, while trimolybdate ones are obtained for OAC-rich reactions.

Against any expectation, the influence of the nature of the OACs on the final products is very poorly documented. Even if the organic component is often considered to play the role of structure-directing agent during the molybdate condensation,[12,13] no concrete correlations between the topologies of both organic and inorganic components have been nowadays established. Only the effect of the charge density of the organic cation on the molybdate composition has been recently approached.[14]

Other features of the OACs should also be considered. For example, because the organic−inorganic interface implies hydrogen-bonding interactions, the N−H bond number of the OACs should be a pertinent parameter to take into account. With this aim, we have initiated exploration of the reactivity of MoO_4^{2-} toward six $^{+}(Me_{3-x}H_xN)(CH_2)_2(NH_yMe_{3-y})^{+}$ ($x, y = 1-3$) OACs, which differ from their N−H bond number per N atom. These cations (hereafter labeled A^{2+} cations), i.e., ethylenediammonium (H_2en^{2+}, $^{+}H_3N(CH_2)_2NH_3^{+}$), methylethylenediammonium (H_2MED^{2+}, $^{+}MeH_2N(CH_2)_2NH_3^{+}$), *N*,*N*′-dimethylethylenediammonium (*N*,*N*′-H_2DMED^{2+}, $^{+}MeH_2N(CH_2)_2NH_2Me^{+}$), *N*,*N*-dimethylethylenediammonium (*N*,*N*-H_2DMED^{2+}, $^{+}Me_2HN(CH_2)_2NH_3^{+}$), *N*,*N*,*N*′-trimethylethylenediammonium ($H_2TriMED^{2+}$, $^{+}Me_2HN(CH_2)_2NH_2Me^{+}$), and *N*,*N*,*N*′,*N*′-tetramethylethylenediammonium (H_2TMED^{2+}, $^{+}Me_2HN(CH_2)_2NHMe_2^{+}$), are depicted in Figure 1. As a preliminary work, we explore in this paper the effect of the synthesis temperature on the different A^{2+}/MoO_4^{2-} systems. Commonly, most of the hybrid materials are obtained using hydrothermal treatments at a fixed temperature, and the effect of this parameter is reported only as a way of improving the crystallinity of the final products. Our goal here is to clearly identify whether the synthesis temperature may impact the composition of hybrid materials. In this context, parameters such as the initial pH, molybdenum concentration, amine/molybdenum ratio, and synthesis duration were taken as constant, while the synthesis temperature was explored in the 70−180 °C range. Our experiments were carried out at initial pH = 2 because of the richness of Mo-POM species accessible in these acidic conditions, including both octamolybdate clusters and chains, trimolybdate chains, and pentamolybdate and heptamolybdate layers.

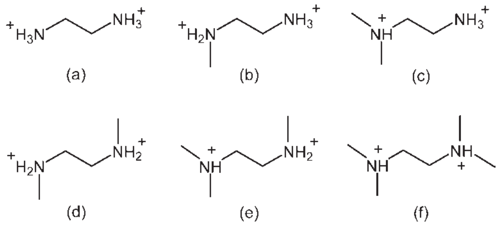

Figure 1. Representation of the six A^{2+} cations with the general formula $^{+}(Me_{3-x}H_xN)(CH_2)_2(NH_yMe_{3-y})^{+}$ (x, y = 1−3): (a) H_2en^{2+}; (b) H_2MED^{2+}; (c) *N*,*N*-H_2DMED^{2+}; (d) *N*,*N*′-H_2DMED^{2+}; (e) $H_2TriMED^{2+}$; (f) H_2TMED^{2+}.

Our work is organized as follows. In section 2, we describe the experimental procedures followed to synthesize 16 hybrid organic−inorganic compounds, namely, $(H_2en)[Mo_3O_{10}]\cdot H_2O$ (**1**), $(H_2en)[Mo_3O_{10}]$ (**2**), $(H_2en)[Mo_5O_{16}]$ (**3**), $(H_2MED)_2[Mo_8O_{26}]\cdot 2H_2O$ (**4**), $(H_2MED)[Mo_5O_{16}]$ (**5**), (*N*,*N*-$H_2DMED)_2[Mo_8O_{26}]\cdot 2H_2O$ (**6**), (*N*,*N*-$H_2DMED)_2[Mo_8O_{26}]\cdot 2H_2O$ (**7**), (*N*,*N*′-$H_2DMED)_2[Mo_8O_{26}]$ (**8**), (*N*,*N*′-$H_2DMED)[Mo_5O_{16}]$ (**9**), $(H_2TriMED)_2[Mo_8O_{26}]\cdot 4H_2O$ (**10**), $(H_2TriMED)_2[Mo_8O_{26}]\cdot 2H_2O$ (**11**), $(H_2TriMED)[Mo_7O_{22}]$ (**12**), $(H_2TMED)_2[Mo_8O_{26}]\cdot 2H_2O$ (**13**), $(H_2TMED)_2[Mo_8O_{26}]$ (**14**), $(H_2TMED)_2[Mo_8O_{26}]$ (**15**), and $(H_2TMED)[Mo_7O_{22}]$ (**16**), as well as the physical techniques used to characterize them. A brief structural description of the eight different Mo-POM blocks in the so-obtained materials is provided in section 3. The details on the supramolecular three-dimensional (3D) networks are given only for new compounds, which gave rise to single-crystal X-ray investigations. The use of Fourier transform (FT)-Raman spectroscopy, as a powerful method to identify the nature of the Mo-POM blocks in the hybrid materials, is also highlighted. The influence of the synthesis temperature on the stabilization of the Mo-POM blocks in the solid state for the six A^{2+}/MoO_4^{2-} systems is discussed in section 4. The essential finding of our work is summarized in section 5. Most of the as-synthesized 16 hybrid materials evidence photochromic properties that we will report elsewhere.

---

(6) Cruywagen, J. J.; Draaijer, A. G.; Heyns, J. B. B.; Rohwer, E. A. *Inorg. Chim. Acta* **2002**, *331*, 322–329.

(7) Tytko, K. H.; Baethe, G.; Cruywagen, J. J. *Inorg. Chem.* **1985**, *24*, 3132–3136.

(8) Coué, V.; Dessapt, R.; Bujoli-Doeuff, M.; Evain, M.; Jobic, S. *J. Solid. State Chem.* **2008**, *181*, 1116–1122.

(9) Nelson, J. H.; Johnston, A. R.; Narducci Sarjeant, A.; Norquist, A. J. *Solid State Sci.* **2007**, *9*, 472–484.

(10) Veltman, T. R.; Stover, A. K.; Narducci Sargeant, A.; Min Ok, K.; Shiv Halasyamani, P.; Norquist, A. J. *Inorg. Chem.* **2006**, *45*, 5529–5537.

(11) Hubbard, D. J.; Johnston, A. R.; Sanchez Casalongue, H.; Narducci Sarjeant, A.; Norquist, A. J. *Inorg. Chem.* **2008**, *47*, 8518–8525.

(12) Upreti, S.; Ramanan, A. *Cryst. Growth Des.* **2005**, *5*, 1837–1843.

(13) Hagrman, P. J.; Hagrman, D.; Zubieta, J. *Angew. Chem., Int. Ed.* **1999**, *38*, 2638–2684.

(14) Casalongue, H. S.; Choyke, S. J.; Narducci Sarjeant, A.; Schrier, J.; Norquist, A. J. *J. Solid State Chem.* **2009**, *182*, 1297–1303.

2. Experimental Section

2.1. Synthesis. Ethylenediamine (en, $N_2C_2H_8$), methylethylenediamine (MED, $N_2C_3H_{10}$), *N*,*N*′-dimethylethylenediamine (*N*,*N*′-DMED, $N_2C_4H_{12}$), *N*,*N*-dimethylethylenediamine (*N*,*N*-DMED, $N_2C_4H_{12}$), *N*,*N*,*N*′-trimethylethylenediamine (TriMED, $N_2C_5H_{14}$), *N*,*N*,*N*′,*N*′-tetramethylethylenediamine (TMED, $N_2C_6H_{16}$), and $Na_2MoO_4 \cdot 2H_2O$ were purchased from Aldrich. All reagents were used without further purification.

Syntheses of Compounds 1−16 from MoO_4^{2-}. A series of 30 experiments were carried out using the starting material $Na_2MoO_4 \cdot 2H_2O$ (0.484 g, 2 mmol) dissolved in 16 mL of water ([Mo] = 0.125 M). After the addition of 2 equiv of the appropriated amine, the pH was adjusted with 5 M HCl to 2.0(1). For syntheses carried out at ambient pressure, the mixtures were systematically stirred for 2 days at 70 °C to enhance the product yields and then filtered to isolate white powders. For syntheses using hydrothermal treatments (i.e., $T > 70$ °C), the initial mixtures were stirred at room temperature for a few minutes and sealed in a 30 mL Teflon-lined autoclave. They were maintained at the desired temperature (i.e., 110, 130, 150, or 180 °C) for 2 days in autogenous pressure conditions. The reactors were then cooled at room temperature, and the final pH was systematically measured. A maximum shift of three tenths was observed. The slurries were then filtered to isolate powders or crystals. All products were obtained pure, with high yield. The detailed synthesis conditions of **1**−**16** are given as S1 in the Supporting Information and are coupled to elemental analyses and differential scanning calorimetry (DSC)/thermogravimetric analysis (TGA) measurements.

In addition to the aforementioned synthesis effort, extra experiments were carried out to shed light on the conversion pathways versus temperature from a given material to another (namely, **1** → **2**, **2** → **3**, **4** → **5**, **6** → **7**, **8** → **9**, **10** → **11**, **11** → **12**, **13** → **14**, **14** → **15**, and **15** → **16**; see section 4). Typically, a powder of compound ***i*** (***i*** = 1, 2, 4, 6, 8, 10, 11, 13, 14, 15) was introduced in an aqueous solution (with [Mo] = 0.125 M), and the pH was adjusted to 2. NaCl was then added to keep the sodium concentration similar to that of the 30 previous experiments. The mixture was sealed in a 30 mL Teflon-lined autoclave and was maintained at a given temperature for 2 days in autogenous pressure conditions. Details are given as S1 in the Supporting Information. In this second set of experiments, a pH increase ranging from 0.05 to 3.6 was observed according to the interconversion reactions of the materials, as expected (see below). Except the transformation of **13** into **14** (both materials containing the same β-$[Mo_8O_{26}]^{4-}$ cluster), which occurs in the solid state by heating of a pure powder of **13** at 150 °C for 4 h in air, all of the other conversions request hydrothermal conditions.

Let us notice that the formulations and purity of the materials were mainly confirmed by the self-consistent results of X-ray diffraction (on single crystal or powder), elemental analysis, FT-Raman spectroscopy, and TGA measurements. When structural information was missing, the purity of the samples and identification of the arrangement of the mineral framework were determined by comparison of the FT-Raman spectra with well-characterized analogues, taking advantage of the chemical analysis.

2.2. Structure Determination. Solvent-free glue was used to firmly fix the crystals at the tip of Lindemann capillaries. Data collections were carried out at room temperature on a Bruker-Nonius Kappa CCD diffractometer using Mo K-$L_{2,3}$ radiation with a graphite monochromator. Intensity integration and standard Lorentz−polarization corrections were done with the *JANA2006* program suite,[15] using crystal shape for absorption correction (the Gaussian method). Direct methods were performed with *SIR2004*,[16] and the charge-flipping method[17,18] was applied using *Superflip*,[19] a built-in part of *JANA2006*. Obtained structures were visualized and plotted with the *Diamond* program.[20] Starting from the model obtained either from direct methods or charge-flipping algorithms (see above), all Mo and O atoms could be located. The C atoms were subsequently found through difference Fourier synthesis. Using anisotropic atomic displacement parameters, the addition of H atoms at calculated positions with angle and distance restraints allowed the refinement to smoothly converge. Residual factors are given in Table 1 for the three structures. CCDC 767408 (**5**), CCDC 767409 (**9**), and CCDC 767410 (**14**) contain the supplementary crystallographic data for this paper. These data can be obtained free of charge via www.ccdc.cam.ac.uk/conts/retrieving.html (or from the Cambridge Crystallographic Data Centre, 12 Union Road, Cambridge CB21EZ, U.K.; fax (44) 1223-336-033; e-mail deposit@ccdc.cam.ac.uk). We have checked the powder purity of these three new materials by a comparison of their patterns with their structures as determined from single crystals (S2−S4 in the Supporting Information).

2.3. Physical Measurements. Powder X-ray diffraction patterns were collected at room temperature on a Siemens D5000 diffractometer without a monochromator (Cu K-$L_{3,2}$), λ = 1.540 598 and 1.544 390 Å; Bragg−Brentano geometry; linear detector; 2θ range = 8−60°. Elemental analyses of the solids were performed by Service d'Analyse du CNRS, Vernaison, France. Raman spectra were collected at room temperature under an excitation wavelength of 1064 nm (Nd:YAG laser) using a FT-Raman Bruker RFS 100 spectrophotometer. The nominal power was modulated between 100 and 340 mW to avoid any degradation of the materials. Spectra were recorded at 4 cm^{-1} resolution over the wavenumber range 100−3500 cm^{-1}, with 1000 scan accumulation. DSC/TGA analyses were measured by flowing dry argon with a heating and cooling rate of 5 °C min^{-1} on a SETARAM TG-DSC 111 between 20 and 800 °C. Such investigations made possible the determination of the thermal stability of the prepared phases, as well as the number of crystallized water molecules in **1**, **4**, **6**, **7**, **10**, **11**, and **13**. The results are given as S5 in the Supporting Information.

3. Hybrid Organic−Inorganic Materials Based on Mo-POMs and A^{2+} Cations

Temperature exploration of the reactivity of six A^{2+}/MoO_4^{2-} systems, at initial pH = 2, leads to the stabilization of 16 hybrid organic−inorganic materials with four general formulas: $(A)_2[Mo_8O_{26}] \cdot xH_2O$ (x = 0, 2, 4), $(A)[Mo_3O_{10}] \cdot xH_2O$ (x = 0, 1), $(A)[Mo_5O_{16}]$, and $(A)[Mo_7O_{22}]$. Four of the prepared materials, i.e., **2**,[21] **3**,[22] **7**,[23] and **15**,[13] were already reported in the literature (but prepared via different synthesis routes). Among the 12 newly prepared materials, three of them have been characterized by single-crystal X-ray diffraction analyses, i.e., **5**, **9**, and **14**. The others, i.e., **1**, **4**, **6**, **8**,

---

[15] Petricek, V.; Dusek, M.; Palatinus, L. *JANA2006, a Crystallographic Computing System*; Institute of Physics, Academy of Sciences of the Czech Republic: Prague, Czech Republic, 2000.

[16] Burla, M. C.; Caliandro, R.; Camalli, M.; Carrozzini, B.; Cascarano, G. L.; De Caro, L.; Giacovazzo, C.; Polidori, G.; Spagna, R. *J. Appl. Crystallogr.* **2005**, *38*, 381–388.

[17] Oszlányi, G.; Suto, A. *Acta Crystallogr., Sect. A: Found. Crystallogr.* **2004**, *60*, 134–141.

[18] Palatinus, L. *Acta Crystallogr., Sect. A: Found. Crystallogr.* **2004**, *60*, 604–610.

[19] Palatinus, L.; Chapuis, G. *J. Appl. Crystallogr.* **2007**, *40*, 786–790.

[20] Brandenburg, K. *Diamond*, version 3; Crystal Impact GbR: Bonn, Germany, 2001.

[21] Khan, I.; Chen, Q.; Zubieta, J. *Inorg. Chim. Acta* **1993**, *213*, 325–327.

[22] Guillou, N.; Ferey, G. *J. Solid. State Chem.* **1999**, *147*, 240–246.

[23] Thorn, K. J.; Narducci Sarjeant, A.; Norquist, A. J. *Acta Crystallogr.* **2005**, *E61*, m1665–m1667.

Table 1. Crystallographic Data for **5**, **9**, and **14**

	5	**9**	**14**
(a) Physical, Crystallographic, and Analytical Data			
empirical formula	$Mo_5O_{16}C_3H_{12}N_2$	$Mo_5O_{16}C_4H_{14}N_2$	$Mo_8O_{26}C_{12}H_{36}N_4$
M_r	811.8	825.9	1419.9
cryst syst, space group	monoclinic, $C2$	monoclinic, $C2/c$	monoclinic, $P2_1/n$
a (Å)	22.8372(13)	22.3577(14)	19.9777(12)
b (Å)	5.591(2)	5.64840(10)	8.4184(5)
c (Å)	14.2472(7)	14.5679(3)	9.9841(6)
β (deg)	120.6990(12)	117.6951(11)	95.592(9)
V (Å^3)	1564.2(6)	1628.94(11)	1671.14(17)
Z	4	4	2
F_{000}	1528	1560	1360
D_x (g cm^{-3})	3.446	3.366	2.821
radiation	Mo K-L$_{2,3}$	Mo K-L$_{2,3}$	Mo K-L$_{2,3}$
λ (Å)	0.710 69	0.710 69	0.710 69
μ (mm^{-1})	3.99	3.83	3.00
T (K)	293	293	293
cryst shape, size	block, white	block, yellowish	block, yellowish
cryst dimens (mm)	0.16 × 0.12 × 0.09	0.29 × 0.13 × 0.03	0.1 × 0.07 × 0.07
(b) Data Collection and Data Reduction			
diffractometer	Nonius CCD	Nonius CCD	Nonius CCD
radiation source	Mo K-L$_{2,3}$	Mo K-L$_{2,3}$	Mo K-L$_{2,3}$
monochromator	graphite	graphite	graphite
scan mode	ω	φ, ω	ω
transmission	$T_{min} = 0.558$, $T_{max} = 0.749$	$T_{min} = 0.492$, $T_{max} = 0.901$	$T_{min} = 0.734$, $T_{max} = 0.834$
measd reflns	27 974	21 665	54 716
indep reflns	6786	4241	7235
reflns with $I > 2\sigma(I)$	6454	3869	6010
abs corrn	Gaussian *JANA2006* (Petricek, Dusek, and Palatinus, 2000)	Gaussian *JANA2006* (Petricek, Dusek, and Palatinus, 2000)	Gaussian *JANA2006* (Petricek, Dusek, and Palatinus, 2000)
R_{int}	0.042	0.035	0.045
θ_{max} (deg)	35.0	35	35.0
θ_{min} (deg)	6.5	6.5	6.5
	$h = -36 \rightarrow 36$, $k = -8 \rightarrow 9$, $l = -22 \rightarrow 22$	$h = -37 \rightarrow 37$, $k = -9 \rightarrow 9$, $l = -24 \rightarrow 24$	$h = -32 \rightarrow 30$, $k = -13 \rightarrow 13$, $l = -16 \rightarrow 15$
(c) Refinement			
refinement	F^2	F^2	F^2
$R[F^2 > 2\sigma(F^2)]$	0.027	0.022	0.030
S	1.30	1.20	1.20
no. of reflns	6786	4241	7235
no. of param	237	124	226
no. of constraints	109	63	72
weighting scheme	$w = 1/[\sigma^2(I) + 0.001936I^2]$	$w = 1/[\sigma^2(I) + 0.001936I^2]$	$w = 1/[\sigma^2(I) + 0.001936I^2]$
$wR(F^2)$	0.078	0.069	0.080
$\Delta\rho_{max}$ (e Å^{-3})	1.20	0.73	0.99
$\Delta\rho_{min}$ (e Å^{-3})	−0.77	−0.75	−0.81
absolute structure	twin components related by a center of symmetry (*JANA2006*)	na	na
extinction corrn	Gaussian isotropic (Becker and Coppens, 1974)	none	none
Flack parameter	0.11(5)	na	na

10−**13**, and **16**, precipitate as white microcrystalline powders and were characterized by vibrational spectroscopies.

3.1. Description of the Mo-POM Blocks in 1−16. X-ray diffraction analyses coupled with FT-Raman spectroscopy show that compounds **1**−**16** contain eight different Mo-POM blocks (FT-Raman spectroscopy has been shown to be more useful in fingerprinting materials than FT-IR spectroscopy because this technique is much less sensitive to deformation implying ions at the border of the mineral block in contact with organic cations). This makes it easier to identify the mineral network with much better resolved spectra compared to the IR ones. Seven of these compounds have the well-known topologies displayed in Figure 2. At the opposite end, the exact topology of Mo-POM in **11** remains unclear (see below).

β-[Mo_8O_{26}]$^{4-}$ Cluster. The β-[Mo_8O_{26}]$^{4-}$ anion (Figure 2a) is a centrosymmetric block composed of eight distorted edge-sharing [MoO_6] octahedra. This well-known discrete cluster has been characterized by X-ray diffraction analysis of **14**. As shown in Figure 3, the β-[Mo_8O_{26}]$^{4-}$

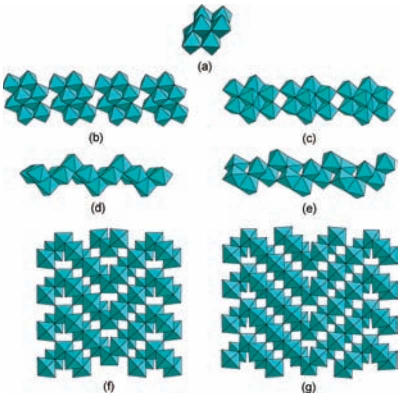

Figure 2. Representations of the seven well-characterized Mo-POM blocks in **1**−**16** except **11**: (a) β-$[Mo_8O_{26}]^{4-}$ clusters; (b) $^1/_\infty[Mo_8O_{26}]^{4-}$ chain type 1; (c) $^1/_\infty[Mo_8O_{26}]^{4-}$ chain type 2; (d) $^1/_\infty[Mo_3O_{10}]^{2-}$ chain type 1; (e) $^1/_\infty[Mo_3O_{10}]^{2-}$ chain type 2; (f) $^2/_\infty[Mo_5O_{16}]^{2-}$ layer; (g) $^2/_\infty[Mo_7O_{22}]^{2-}$ layer.

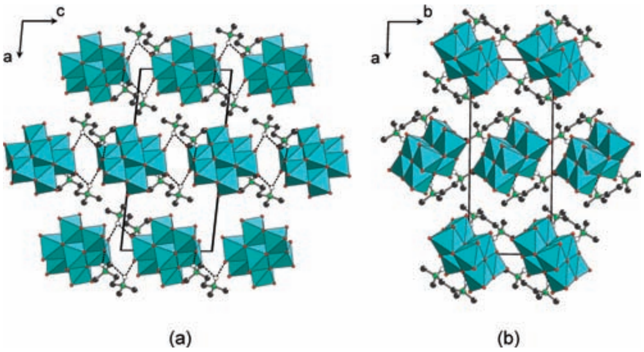

Figure 3. Projections of the supramolecular 3D network in **14** perpendicular to the (a) *ac* and (b) *ab* planes. The discrete β-$[Mo_8O_{26}]^{4-}$ entities link the H_2TMED^{2+} cations via hydrogen-bonding interactions (depicted as dotted lines) to form infinite $^1/_\infty\{(H_2TMED)_2[Mo_8O_{26}]\}$ chains running along the *c* axis. For clarity, the H atoms of the CH_2 and CH_3 groups are omitted.

blocks are connected to each other by two H_2TMED^{2+} cations via hydrogen-bonding interactions (see Table 2) to form infinite $^1/_\infty\{(H_2TMED)_2[Mo_8O_{26}]\}$ chains running along the *c* axis. These chains are maintained parallel via van der Waals and electrostatic interactions to give rise to a supramolecular 3D network.

Infinite $^1/_\infty[Mo_8O_{26}]^{4-}$ Chain. This polymeric block exists under the form of two isomers hereafter labeled type 1 (Figure 2b) and type 2 (Figure 2c). Both are built from the similar $[Mo_8O_{28}]$ subunit, based on eight edge-shared distorded $[MoO_6]$ octahedra connected via the sharing of two common vertices. The two isomers only differ by the connection modes of the $[Mo_8O_{28}]$ blocks (see Figure 2). The types 1 and 2 $^1/_\infty[Mo_8O_{26}]^{2-}$ chains have been well identified by single-crystal X-ray diffraction analyses in **7** and **15**, respectively.

Infinite $^1/_\infty[Mo_3O_{10}]^{2-}$ Chain. The $^1/_\infty[Mo_3O_{10}]^{2-}$ chain is another polymeric block with two different isomers, namely, type 1 (Figure 2d) and type 2 (Figure 2e). Both trimolybdate blocks are built upon $[MoO_6]$ octahedra with different connection modes. These octahedra are edge-shared and corner-shared in type 1 and corner-, edge-, and face-shared in type 2. The type 2 $^1/_\infty[Mo_3O_{10}]^{2-}$ chains have been well detected by single-crystal X-ray diffraction analysis in **2**.

Table 2. Hydrogen-Bonding Geometry (Å and deg) in **5**, **9**, and **14**[a]

$N-H\cdots O$	$H\cdots O$	$N\cdots O$	$N-H\cdots O$
	Compound **5**		
$N_1-H_2\cdots O_{12}$	1.929	2.783(5)	153.53
$N_1-H_3\cdots O_{16}$	1.917	2.755(7)	150.36
$N_2-H_8\cdots O_4$*	1.963	2.810(6)	152.06
$N_2-H_9\cdots O_{13}$	2.256	2.885(5)	125.01
$N_2-H_8\cdots O_7$*	2.220	2.759(6)	116.7
	Compound **9**		
$N_1-H_1\cdots O_1$	1.857	2.729(3)	157.31
$N_1-H_2\cdots O_7$	2.240	2.899(2)	128.09
	Compound **14**		
$N_1-H_{1N1}\cdots O_7$	2.26	2.995(3)	136.56
$N_1-H_{1N1}\cdots O_4$	2.238	2.896(3)	119.80
$N_1-H_{1N1}\cdots O_2$	2.234	2.875(3)	126.27
$N_2-H_{1N2}\cdots O_3$	2.019	2.990(3)	149.97

[a] The asterisk indicates a possible hydrogen bonding whose existence depends on the accurate location of the H atom.

$^2/_\infty[Mo_5O_{16}]^{2-}$ and the $^2/_\infty[Mo_7O_{22}]^{2-}$ Layers. Both the $^2/_\infty[Mo_5O_{16}]^{2-}$ and $^2/_\infty[Mo_7O_{22}]^{2-}$ entities are less frequent two-dimensional (2D) Mo-POM block. The pentamolybdate block (Figure 2f) has been characterized from single-crystal X-ray diffraction analyses in **5** and **9** associated with H_2MED^{2+} and *N*,*N'*-H_2DMED^{2+} cations, respectively. This inorganic layer has already been described by Gatehouse and Miskin[24] in terms of infinite $[MoO_4]$ ribbon blocks with ReO_3-type structure. These one-dimensional (1D) blocks are five octahedra wide and one octahedron thick and are connected to each other by the sharing of octahedron edges, as displayed in Figure 4a. The arrangement between the organic and inorganic components is similar in both **5** and **9** (Figure 4b,c); that is, the $^2/_\infty[Mo_5O_{16}]^{2-}$ layers are stacked along the *a* axis and are pillared by the A^{2+} cations. The two ammonium head groups of the cations develop hydrogen-bonding interactions with specific O atoms of the inorganic layer (see Table 2). The topology of the $^2/_\infty[Mo_7O_{22}]^{2-}$ layer (Figure 2g) is similar to that of the $^2/_\infty[Mo_5O_{16}]^{2-}$ block, except that the $[MoO_4]$ ribbons are seven octahedra wide and one octahedron thick. This block has been well characterized only in a few hybrid organic−inorganic materials such as $(CH_3NH_3)_2[Mo_7O_{22}]$.[25]

3.2. Characterization of the Mo-POM Blocks in 1−16 by FT-Raman Spectroscopy. As aforementioned, FT-Raman spectroscopy appears as an appropriate and powerful method to identify the nature of the Mo-POM blocks in **1**−**16**, especially for materials containing different Mo-POM isomers. Figure 5 shows a comparison between the Raman spectra of **7**, **11**, **14**, and **15** in the 1200−200 cm^{-1} range, which contains the absorption bands relative to the mineral components. Practically, this domain may be restricted to the 890−600 cm^{-1} range to unambiguously and pragmatically discriminate the four octamolybdate isomers in **7**, **11**, **14**, and **15**. In this context, the spectrum of the β-$[Mo_8O_{26}]^{4-}$ cluster in **14** shows only two absorption bands at 859 and 832 cm^{-1} (Figure 5a). In

---

(24) Gatehouse, B. M.; Miskin, B. K. *Acta Crystallogr.* **1975**, *B31*, 1293–1299.

(25) Zavalij, P. Y.; Whittingham, M. S. *Acta Crystallogr.* **1997**, *C53*, 1374–1376.

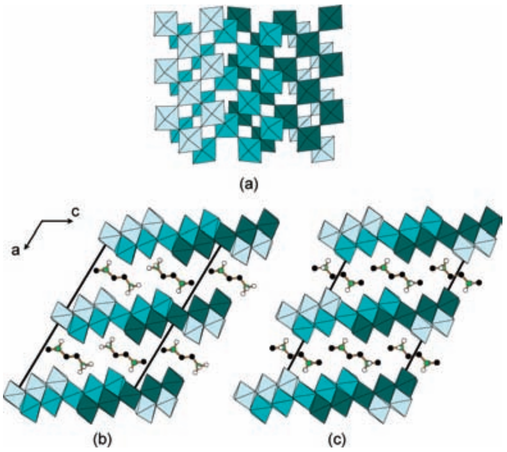

Figure 4. (a) Schematic stacking of the [MoO_4] ribbons with ReO_3-type structure to form the $^{2}/_{\infty}[Mo_5O_{16}]^{2-}$ layer. Representation of the arrangement between the $^{2}/_{\infty}[Mo_5O_{16}]^{2-}$ layers and (b) the H_2MED^{2+} cations in **5** and (c) the *N*,*N*′-H_2DMED^{2+} cations in **9**. For clarity, the H atoms of the CH_2 and CH_3 groups are omitted.

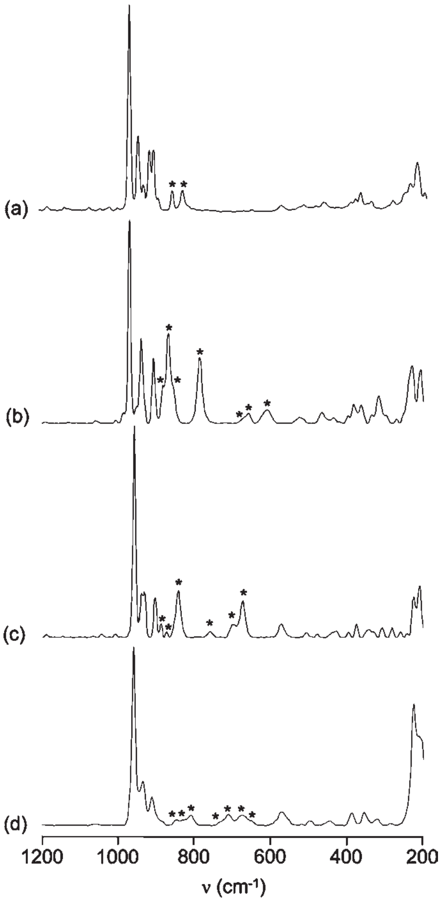

Figure 5. Comparison of the Raman signatures of (a) the β-$[Mo_8O_{26}]^{4-}$ cluster in **14**, (b) the $^{1}/_{\infty}[Mo_8O_{26}]^{4-}$ chain type 1 in **7**, (c) the $^{1}/_{\infty}[Mo_8O_{26}]^{4-}$ chain type 2 in **15**, and (d) the unidentified octamolybdate block in **11**. Asterisks denote the absorption bands characteristic of the different Mo-POM blocks in the 890−600 cm^{-1} range.

the same range, the spectrum of the type 1 $^{1}/_{\infty}[Mo_8O_{26}]^{4-}$ chains in **7** shows seven absorption bands located at 884, 868, 855, 787, 679, 662, and 614 cm^{-1} (Figure 5b), and the one of the type 2 $^{1}/_{\infty}[Mo_8O_{26}]^{4-}$ chains in **15** shows six absorption bands at 889, 874, 843, 760, 700, and 673 cm^{-1} (Figure 5c). The FT-Raman signature of the octamolybdate block in **11** differs from the three other isomers with eight distinguishable absorption bands at 890, 853, 834, 814, 735, 716, 681, and 654 cm^{-1} (Figure 5d). In fact, the $[Mo_8O_{26}]^{4-}$ entity is a flexible block that can adopt numerous different geometries. For example, the isolated $[Mo_8O_{26}]^{4-}$ cluster has been characterized in the solid state into nine isomers, namely, α,[26,27] β,[28−30] γ,[31−33] δ,[34−37] ε,[38] ζ,[39,40] ξ,[41] η,[42] and θ.[43,44] Because of the lack of Raman characterizations for these species, the topology of the octamolybdate block in **11** cannot be precisely identified. Nevertheless, we may suppose that **11** contains one of the aforementioned species, bare β-$[Mo_8O_{26}]^{4-}$ and δ-$[Mo_8O_{26}]^{4-}$ isomers whose absorption lines do not coincide (see S6 in the Supporting Information).

On the basis of FT-Raman spectroscopy, the β-$[Mo_8O_{26}]^{4-}$ cluster is suspected in **6**, **10**, and **13** from a comparison of their spectra with the one of **14** (see S7 in the Supporting Information). In the same way, the type 1 $^{1}/_{\infty}[Mo_8O_{26}]^{4-}$ chain has also been evidenced in **4** and **8** by a comparison of their Raman spectra with that of **7** (see S8 in the Supporting Information). Finally, both type 1 (in **1**) and type 2 (in **2**) $^{1}/_{\infty}[Mo_3O_{10}]^{2-}$ chains are perfectly distinguishable by FT-Raman spectroscopy. The absorption bands relative to the type 1 $^{1}/_{\infty}[Mo_3O_{10}]^{2-}$ chain in **1** match very well those of $(H_2DABCO)[Mo_3O_{10}]\cdot H_2O$[4] (see S9 in the Supporting Information).

The FT-Raman signatures of both the $^{2}/_{\infty}[Mo_5O_{16}]^{2-}$ and $^{2}/_{\infty}[Mo_7O_{22}]^{2-}$ layers are also perfectly distinguishable. Figure 6 displays a comparison between the Raman spectra of **9**, $(CH_3NH_3)_2[Mo_7O_{22}]$, **12**, and **16** in the 1200−200 cm^{-1} range. All spectra show two sets of absorption bands. The first one in the 850−200 cm^{-1} range contains weak absorption bands, common for the four materials. The second set, in the 1000−850 cm^{-1} range, contains strong and medium absorption bands and

---

(26) Hagrman, D.; Hagrman, P.; Zubieta, C. *Inorg. Chim. Acta* **2000**, *300−302*, 212–224.

(27) Kalpana, G.; Vidyasagar, K. *Acta Crystallogr.* **2005**, *E61*, m1885–m1886.

(28) Muller, E. A.; Narducci Sarjeant, A.; Norquist, A. J. *Acta Crystallogr.* **2005**, *E61*, m730–m732.

(29) Gili, P.; Nunez, P.; Martin-Zarza, P.; Lorenzo-Luis, P. A. *Acta Crystallogr.* **2000**, *C56*, e441–e442.

(30) Li, Q.; Zhang, S.-W. Z. *Allg. Chem.* **2005**, *631*, 645–648.

(31) Niven, M. L.; Cruywagen, J. J.; Heyns, J. B. B. *J. Chem. Soc., Dalton Trans.* **1991**, *8*, 2007–2011.

(32) Rarig, R. S., Jr.; Zubieta, J. *Polyedron* **2003**, *22*, 177–188.

(33) Cui, X.-B.; Lu, K.; Fan, Y.; Xu, J.-Q.; Ye, L.; Sun, Y.-H.; Li, Y.; Yu, H.-H.; Yi, Z.-H. *J. Mol. Struct.* **2005**, *743*, 151–155.

(34) Coué, V.; Dessapt, R.; Bujoli-Doeuff, M.; Evain, M.; Jobic, S. *J. Solid State Chem.* **2006**, *179*, 3601–3613.

(35) Rarig, R. S., Jr.; Zubieta, J. *Inorg. Chim. Acta* **2001**, *312*, 188–196.

(36) Xiao, D.; An, H.; Wang, E.; Xu, L. *J. Mol. Struct.* **2005**, *738*, 217–225.

(37) Burkholder, E.; Zubieta, J. *Inorg. Chim. Acta* **2005**, *358*, 116–122.

(38) Hagrman, D.; Zubieta, C.; Rose, D. J.; Zubieta, J.; Haushalter, R. C. *Angew. Chem., Int. Ed. Engl.* **1997**, *36*, 873–876.

(39) Burkholder, E.; Zubieta, J. *Solid State Sci.* **2004**, *6*, 1421–1428.

(40) Allis, D. G.; Rarig, R. S.; Burkholder, E.; Zubieta, J. *J. Mol. Struct.* **2004**, *688*, 11–31.

(41) Xu, J.-Q.; Wang, R.-Z.; Yang, G.-Y.; Xing, Y.-H.; Li, D.-M.; Bu, W.-M.; Ye, L.; Fan, Y.-G.; Yang, G.-D.; Xing, Y.; Lin, Y.-H.; Jia, H.-Q. *Chem. Commun.* **1999**, 983–984.

(42) Rarig, R. S.; Bewley, L.; Burkholder, E.; Zubieta, J. *Indian J. Chem.* **2003**, *42A*, 2235–2243.

(43) Allis, D. G.; Burkholder, E.; Zubieta, J. *Polyhedron* **2004**, *23*, 1145–1152.

(44) Xiao, D.; Hou, Y.; Wang, E.; Wang, S.; Li, Y. L.; Xu, C. H. *Inorg. Chim. Acta* **2004**, *357*, 2525–2531.

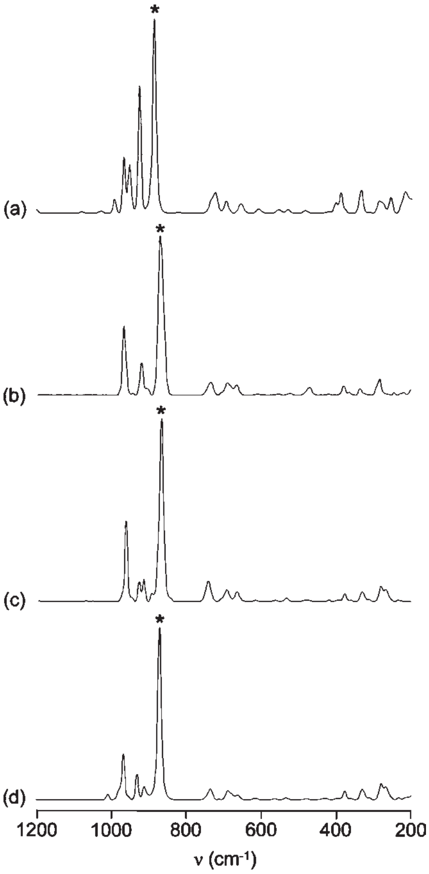

Figure 6. Comparison of the FT-Raman signatures of (a) the $^{2}/_{\infty}[Mo_5O_{16}]^{2-}$ layer in **9** and the $^{2}/_{\infty}[Mo_7O_{22}]^{2-}$ layer in (b) **12**, (c) **16**, and (d) $(CH_3NH_3)_2[Mo_7O_{22}]$.

allows discrimination of the two Mo-POM layers. The $^{2}/_{\infty}[Mo_5O_{16}]^{2-}$ block in **9** is notably characterized by a strong absorption band located at 886 cm^{-1} (Figure 6a; in comparison, the latter is observed at 884 cm^{-1} in **5** and 885 cm^{-1} in **3**). The Raman spectra of $(CH_3NH_3)_2[Mo_7O_{22}]$ (Figure 6d), **12** (Figure 6b), and **16** (Figure 6c) show that this absorption band arises at lower frequency, at 870, 871, and 868 cm^{-1} respectively.

A detailed analysis of the Raman spectra with the aim of correlating the absorption bands to the specific vibrational modes of the different Mo-POM blocks is currently in progress.

4. Influence of the Temperature on the Stabilization of the Mo-POM Blocks in the Solid State

Figure 7 shows an unprecedented diagram built from the series of 30 experiments described in section 2. The diagram displays five concentric hexagons, each of them being associated with a given synthesis temperature (i.e., 70 °C for the smallest hexagon and 180 °C for the largest one). Each hexagon is now divided into six equal portions devoted to each of the six A^{2+}/MoO_4^{2-} investigated systems. To each of the 30 as-defined domains is then associated a specific material (namely, **1**−**16**) obtained as a pure sample with a high yield (see S1 in the Supporting Information) for a given (temperature, A^{2+} cation) couple. The color of each domain indicates the nature of the Mo-POM blocks stabilized in the quoted material. The octamolybdate block is the more frequently met mineral entity in the diagram and is observed in 17 of the 30 domains.

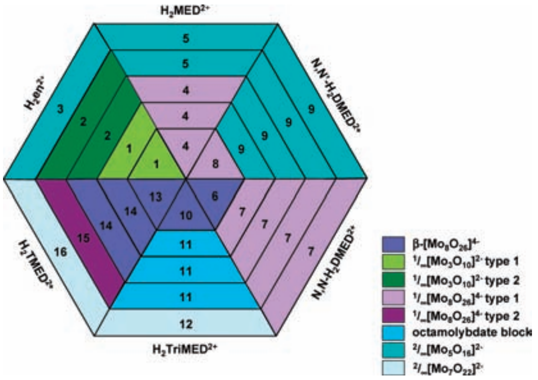

Figure 7. Diagram showing the influence of the synthesis temperature on the Mo-POM block composition of **1**−**16** in the six A^{2+}/MoO_4^{2-} systems. The five concentric hexagons depict the different synthesis temperatures, in the sequence 70, 110, 130, 150, and 180 °C from the smallest one to the largest one. All syntheses with temperatures up to 70 °C were carried out using hydrothermal treatments.

The trimolybdate, pentamolybdate, and heptamolybdate blocks occupy four, seven, and two domains, respectively.

As we expected, the diagram shows that, for a given temperature, the nature of the Mo-POM blocks stabilized in the solid state varies in the different A^{2+}/MoO_4^{2-} systems, which unambiguously illustrates the influence of the N−H bond number per N atom of the A^{2+} cations on the molybdate condensation. In addition, the diagram shows that the reactivity of MoO_4^{2-} toward the A^{2+} cations differs by varying the synthesis temperature. It presumes that the **1**−**16** materials are stable only in well-defined temperature ranges. We confirm this assertion by carrying out conversion of **1** → **2**, **2** → **3**, **4** → **5**, **6** → **7**, **8** → **9**, **10** → **11**, **11** → **12**, **13** → **14**, **14** → **15**, and **15** → **16** under hydrothermal conditions, at temperatures deduced from Figure 7. These experiments highlight that a material *i* is converted to a material *j* beyond a specific temperature. These conversions should occur through dissolution−crystallization processes, with in most cases a rearrangement of the Mo-POM blocks. So, our work clearly evidences that stabilization of the Mo-POM blocks in the solid state is temperature-dependent.

The synthesis temperature impacts both the composition and topology of the Mo-POM blocks. The molybdate composition evolves with an increase in the synthesis temperature according to different sequences, which depend on the A^{2+} cations. These sequences are as follows: $^{1}/_{\infty}[Mo_8O_{26}]^{4-}$ (type 1) < $^{2}/_{\infty}[Mo_5O_{16}]^{2-}$ for $A^{2+} = H_2MED^{2+}$ and N,N'-H_2DMED^{2+}; β-$[Mo_8O_{26}]^{4-}$ < $^{1}/_{\infty}[Mo_8O_{26}]^{4-}$ (type 1) for $A^{2+} = N,N$-H_2DMED^{2+}; β-$[Mo_8O_{26}]^{4-}$ < $^{1}/_{\infty}[Mo_8O_{26}]^{4-}$ (type 2) < $^{2}/_{\infty}[Mo_7O_{22}]^{2-}$ for $A^{2+} = H_2TMED^{2+}$; β-$[Mo_8O_{26}]^{4-}$ < $[Mo_8O_{26}]^{4-}$ (unknown) < $^{2}/_{\infty}[Mo_7O_{22}]^{2-}$ for $A^{2+} = H_2TriMED^{2+}$; $^{1}/_{\infty}[Mo_3O_{10}]^{2-}$ (type 1) < $^{1}/_{\infty}[Mo_3O_{10}]^{2-}$ (type 2) < $^{2}/_{\infty}[Mo_5O_{16}]^{2-}$ for $A^{2+} = H_2en^{2+}$. The dimensionality of the Mo-POM blocks in the six A^{2+}/MoO_4^{2-} systems tends to increase from 0D to 1D or from 1D to 2D with an increase in the synthesis temperature, even if some uncertainty remains for the $H_2TriMED^{2+}/MoO_4^{2-}$ system, because of the undetermined topology of the Mo-POM block in **11**.

The isomerization between the β-$[Mo_8O_{26}]^{4-}$ cluster and the infinite $^{1}/_{\infty}[Mo_8O_{26}]^{4-}$ chain is theoretically pH-independent, and we observe no significant variations of the pH values after conversions of **6** into **7** at 110 °C and **14** into **15** at 150 °C. On the other hand, conversions of both $^{1}/_{\infty}[Mo_8O_{26}]^{4-}$

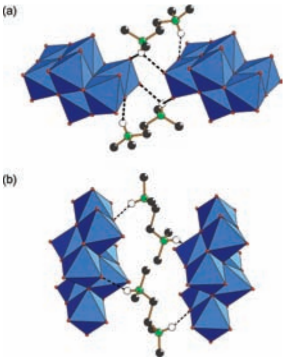

Figure 8. Representation of the hydrogen-bonding interfaces between the H_2TMED^{2+} cations and two adjacent Mo-POM blocks in (a) **14** and (b) **15**, showing the two distinct conformations of the H_2TMED^{2+} cations. The type 2 $^1/_\infty[Mo_8O_{26}]^{4-}$ chains in **15** are limited to the $[Mo_8O_{28}]$ subunits. For clarity, the H atoms of the CH_2 and CH_3 groups are omitted.

and $^1/_\infty[Mo_3O_{10}]^{2-}$ chains into the $^2/_\infty[Mo_5O_{16}]^{2-}$ layers, as well as conversion of the $^1/_\infty[Mo_8O_{26}]^{4-}$ chains into the $^2/_\infty[Mo_7O_{22}]^{2-}$ layers are all proton-consuming, according to the formal equations 1−3. This is in agreement with the strong increase of the pH values observed after the syntheses of **5** from **4** at 150 °C, **9** from **8** at 110 °C, and **3** from **2** at 180 °C and the ones of **12** and **16** from **11** and **15**, respectively, at 180 °C (see S1 in the Supporting Information). The evolutions of the octamolybdate and trimolybdate blocks to the pentamolybdate or heptamolybdate blocks by simply increasing the synthesis temperature show unambiguously that the higher the synthesis temperature, the more acidic the stabilized Mo-POM block. At this stage, it is worth noticing that the large aforementioned pH shifts can be annihilated by realizing the interconversion reactions in a glycine/HCl-buffered solution at pH = 2.0.

$$5[Mo_8O_{26}]^{4-} + 4H^+ \leftrightarrows 8[Mo_5O_{16}]^{2-} + 2H_2O \qquad (1)$$

$$5[Mo_3O_{10}]^{2-} + 4H^+ \leftrightarrows 3[Mo_5O_{16}]^{2-} + 2H_2O \qquad (2)$$

$$7[Mo_8O_{26}]^{4-} + 12H^+ \leftrightarrows 8[Mo_7O_{22}]^{2-} + 6H_2O \qquad (3)$$

In addition, we point out the influence of the synthesis temperature on the topology of Mo-POM isomers, which is particularly well illustrated in the H_2TMED^{2+}/MoO_4^{2-} system. **14** and **15** have exactly the same composition but differ from the topology of the octamolybdate blocks. **14** contains the β-$[Mo_8O_{26}]^{4-}$ cluster, while **15** contains the infinite type 2 $^1/_\infty[Mo_8O_{26}]^{4-}$ chains. According to Figure 7, **14** is stable from 110 to 130 °C and then converts into **15** at 150 °C. Figure 8 depicts the organic−inorganic interfaces in both materials. The flexible H_2TMED^{2+} cation adopts two different conformations, which differ from the position of the H atoms of the two N−H bonds toward a pseudoplane, containing the two N atoms and the two C atoms of the central ethylene group. The H atoms are localized on the same side and on both sides of the plane in **14** and **15**, respectively. No change of the size of the H_2TMED^{2+} cation is observed between the two conformations.

Hence, stabilization of the type 2 $^1/_\infty[Mo_8O_{26}]^{4-}$ chains in **15** can not only be attributed to the nature of the H_2TMED^{2+} cation, because the latter can modify its shape to stabilize the β-$[Mo_8O_{26}]^{4-}$ cluster in **14** for temperatures in the 110−130 °C range. From these results, we underline the absolute necessity to systematically define a couple of parameters, i.e., the nature of the OAC and the temperature to characterize a specific Mo-POM block.

5. Concluding Remarks

To summarize, the reactivity of MoO_4^{2-} toward the six A^{2+} cations leads to 16 hybrid organic−inorganic materials containing 8 different Mo-POM blocks, perfectly distinguishable by FT-Raman spectroscopy. From our phase diagram, we point out that the N−H bond number per N atom of the A^{2+} cations impacts the design of the hybrid materials. The correlation between stabilization of the Mo-POM blocks and this parameter is under study. In addition, we highlight that, for a given experimental setting (initial pH, molybdenum concentration, nature of the A^{2+} cation, and organic/molybdenum ratio), the synthesis temperature is unambiguously a pertinent chemical lever to take into account to direct both the composition and topology of the Mo-POM blocks in hybrid materials. Notably, **1**−**16** materials are stable in specific temperature ranges, and their thermal conversions occur in most cases with an increase of the molybdate dimensionality, from isolated clusters to infinite chains and layers. Finally, we establish that attempts to correlate the topology of the Mo-POM block to the structure of a specific OAC should not be achieved without a preliminary complete temperature investigation of the OAC/MoO_4^{2-} system. We hope our results will offer promising perspectives to better anticipate the design of new hybrid organic−inorganic materials.

Acknowledgment. This work was supported by CNRS and by Ministère de l'Education Nationale, de l'Enseignement Supérieur et de la Recherche. The authors are also indebted to Groupe LAPEYRE for its financial support.

Supporting Information Available: Syntheses of **1**−**16**, single-crystal X-ray diffraction patterns, determination of the number of crystallized water molecules, and Raman spectra. This material is available free of charge via the Internet at http://pubs.acs.org.